

Scaling relations and tidal disruption in spin s ultralight dark matter models

Jessica N. López-Sánchez,¹★ Erick Munive-Villa,¹† Constantinos Skordis^{1,2}‡ Federico R. Urban¹§

¹*CEICO—FZU, Institute of Physics of the Czech Academy of Sciences, Na Slovance 1999/2, 182 00 Prague, Czech Republic*

²*Department of Physics, University of Oxford, Denys Wilkinson Building, Keble Road, Oxford OX1 3RH, UK*

Accepted XXX. Received YYY; in original form ZZZ

ABSTRACT

We explore the impact of spin 0, spin 1 and spin 2 Ultra-Light Dark Matter (ULDM) on small scales by numerically solving the Schrödinger-Poisson system using the time-split method. We perform simulations of ULDM for each spin, starting with different numbers of identical initial solitons and analyse the properties of the resulting halos after they merge and relax in a steady-state. Our findings reveal that higher spin values lead to broader, less dense final halo with more prominent Navarro-Frenk-White (NFW) tails, a characteristic that persists regardless of the number of initial solitons involved. We identify scaling relations that describe the density profile, core and NFW tail of spin s ULDM halos as a function of the number of initial solitons N_{sol} . These relations allow us to construct equivalent halos based on average density or total mass, for arbitrarily large N_{sol} , without having to simulate those systems. We simulate the orbit of a ULDM satellite in a constructed halo treated as an external potential, and find that for host halos having the same average density, the orbital decay time of the satellite is as predicted for uniform sphere host halo regardless of the spin. However, satellites orbiting haloes having the same mass for each spin, result in faster disruption in the case of spin 0, while satellites orbiting haloes having the same core size result in faster disruption in the case of spin 2.

Key words: dark matter – galaxies: structure

1 INTRODUCTION

Ultra-light dark matter (ULDM), namely bosonic dark matter particles whose mass is of order 10^{-22} eV, has been established as a viable and phenomenologically rich candidate for the observed cosmological dark matter (Niemeyer 2020). ULDM is modelled as an oscillating classical field minimally coupled to gravity, existing as a superposition of nearly coherent waves, with spin 0 (scalar field) (Ferreira 2021; Hu et al. 2000; Matos et al. 2000), spin 1 (vector field) or spin 2 (tensor field) (Jain & Amin 2022; Alexander et al. 2021). In these models, provided the mass is sufficiently small, the de Broglie wavelength is of the order of kiloparsecs, the typical size of observable galaxies in the Universe. The result is an effective ‘quantum pressure’ that counteracts gravitational attraction which then has an impact on the formation and distribution of structures at small scales.

ULDM may be compared to Cold Dark Matter (CDM) which is a collision-less cold fluid that forms self-bound, virialised units called halos through a hierarchical process. Both ULDM and CDM predict the formation of large-scale structures in the Universe in concordance with observations from cosmological surveys at large scales. However, ULDM may have an edge when confronted with observations at small scales, where CDM predictions seem to be in tension with the data (Bullock & Boylan-Kolchin 2017; Del Popolo

& Le Delliou 2017)—see also Feng (2010); Bertone & Tait (2018); Tulin & Yu (2018) for an overview of the alternatives.

While spin 0 ULDM has been the subject of investigation over the last two decades, the study of higher spin ULDM using both analytic and numerical methods is more recent. Small-scale simulations of solitonic configurations for spin 0 and spin 1 ULDM were contrasted in Amin et al. (2022), where it was shown that the central region of solitons in spin 1 ULDM is less dense and has a smoother transition as the radius increases compared to the spin 0 case. Additionally, it was found that solitons for spin 1 and spin 2 are formed later than for the spin 0 case, that is, the higher the spin, the larger the soliton condensation time (Jain et al. 2023). In all cases, the solitons are surrounded by a Navarro-Frenk-White (NFW) envelope connected to other filamentary structures (Gorghetto et al. 2022; Jain et al. 2023; Chen et al. 2023). These results show differences between each model in simple configuration ensembles, which can give rise to significant observable effects. Two such effects concern the dynamics of satellite subhalo systems within a host halo, specifically, their tidal disruption and the effect of dynamical friction.

The tidal disruption of subhalos has been extensively explored only in the case of spin 0 ULDM. In Hui et al. (2017), the tidal radius of a spin 0 ULDM satellite was estimated using a spherically symmetric tidal potential $\propto r^2$ (centred around the satellite) using the time-independent Schrödinger-Poisson system (SP). It was shown that spin 0 ULDM within the tidal radius can escape to infinity by tunnelling through the potential barrier at the tidal radius, implying that all systems subjected to an external tidal field will eventually be disrupted. The survival time of a satellite subhalo depends on the

★ E-mail: lopez@fzu.cz

† E-mail: munive@fzu.cz

‡ E-mail: skordis@fzu.cz

§ E-mail: federico.urban@fzu.cz

ratio of its central density to the average density of host halo over the orbital radius of the satellite. It was found that larger such ratios result in more circular orbits before disruption happens. The time-independent approximation to the SP system was questioned in [Du et al. \(2018\)](#) where it was seen to be valid only for small enough times. Considering time dependence and still within the $\propto r^2$ tidal potential model, it was found that the core loses mass faster and becomes increasingly susceptible to tidal effects, leading to faster disruption times. Increasing the model complexity, [Du et al. \(2018\)](#) also performed full three-dimensional numerical simulations for determining the time-dependent profile of a spin 0 ULDM satellite moving in a host halo modelled as a uniform sphere with a fixed mass and treated as an external potential. In this case, the satellite loses mass gradually and quickly relaxes to a less compact configuration, which can be described by a new soliton with lower central density. Using their numerical simulations, [Du et al. \(2018\)](#) then estimated the survival time of satellite galaxies in the Milky Way.

The dynamical friction acting on satellites traversing a host halo in spin 0 ULDM has been studied in [Hui et al. \(2017\)](#) to address the puzzling existence of globular clusters in the Fornax dwarf spheroidal satellite of the Milky Way. In the case of CDM, considering the model's predictions due to dynamical friction, it is unexpected to have long orbital decay times since the system merges quickly to the center. However, when taking satellites as point masses moving within an ULDM halo, the authors estimated that their orbital decay time is always longer than in the case of CDM, thus offering a possible resolution. However, in ULDM the satellite profile can be important as dynamical friction receives contributions from scales comparable to the solitonic core ([Hui et al. 2017](#)). A thorough exploration of dynamical friction in spin 0 ULDM was performed in [Lancaster et al. \(2020\)](#), where apart from a point-mass, the case of an extended satellite profile described by a Plummer sphere was considered and further placed within an ULDM halo with velocity dispersion. They showed that overdensities in the ULDM condensate disrupt the gravitational wake, decreasing the effect of dynamical friction compared to setups without velocity dispersion. In another study, [Vitsos & Gourgoulatos \(2023\)](#) considered satellites in a spin 0 ULDM halo described again by an external potential but which depart from spherical symmetry, inspired by the fact that satellites do not necessarily have perfectly spherical profiles in the observable Universe. They reported that the shape of the wake that the satellite creates on the host halo depends strongly on the satellite's ellipticity and direction of motion.

The study of the dynamics between satellite galaxies and their host halos within alternative dark matter models and examining their effects on survival time, structural configurations and mass transfer, can reveal significant differences that can be compared with observational data. Specifically, one may ask how the satellite dynamics changes for ULDM models with different spin s . In this work, we investigate the properties of halos formed through the mergers of soliton configurations, characterising their density profiles using universal scaling relations. We then apply these findings to model the dynamics of a satellite within a realistic external potential that we numerically compute for a spin s ULDM halo using the SP system. By considering spin 0, spin 1 and spin 2 ULDM, we aim to distinguish the effects specifically attributed to having additional degrees of freedom arising from the different ULDM spins.

The paper is organised as follows: in Section 2, we discuss the non-relativistic modelling of ULDM, focussing on the multi-component Schrödinger-Poisson system for spin 0, spin 1 and spin 2. Section 3 provides a brief overview of the numerical methods employed to evolve the system of equations in each model. In Section 4 we report

on the results of multiple soliton mergers of each spin s model in order to explore the evolution and properties of the resultant halo, including the density profile, total energy and spin density. In section 5, we identify scaling relations between the initial density profile of the solitons and the density profile of the final soliton, corresponding to a final halo profile, created through their merging. This allows us to construct ULDM halos with the equivalent properties for each model. In section 6, we apply the resultant dark matter profiles to use them as host halos of satellite systems. In this case, the host halo is made of spin 0, spin 1 or spin 2 and is considered an external potential. We summarise our conclusions in Section 7.

2 NON-RELATIVISTIC APPROACH FOR SPIN S ULDM

A spin s massive field in the non-relativistic limit can be described by the multiple-component SP system ([Jain & Amin 2022](#); [Adshad & Lozanov 2021](#))

$$\begin{aligned} i\hbar \frac{\partial}{\partial t} \Psi &= -\frac{\hbar^2}{2m_s} \nabla^2 \Psi + m_s \Phi \Psi, \\ \nabla^2 \Phi &= 4\pi G \rho_0 (\text{Tr}[\Psi^\dagger \Psi] - 1), \end{aligned} \quad (1)$$

where \hbar stands for the reduced Planck constant, G is the gravitational constant, m_s is the mass of the ULDM particle and ρ_0 is the mean density of the simulation. We have normalised the wavefunction to the mean density on the simulation so that $\langle \text{Tr}[\Psi^\dagger \Psi] \rangle = 1$ and $\text{Tr}[\Psi^\dagger \Psi]$ is the probability density of occupation. Throughout this section, we use the notation in [Jain & Amin \(2022\)](#) to construct the initial conditions of the simulations. Then, the field is expressed as a function of the spin as follows:

$$\begin{aligned} \psi &= [\Psi] && \text{spin 0,} \\ \psi_i &= [\Psi]_i && \text{spin 1,} \\ \psi_{ij} &= [\Psi]_{ij} && \text{spin 2.} \end{aligned} \quad (2)$$

The trace is defined as $\text{Tr}[\Psi\Psi^\dagger] = \psi_i\psi_i^\dagger$ and $\text{Tr}[\Psi\Psi^\dagger] = \psi_{ij}\psi_{ji}^\dagger$ for spin 1 and spin 2, respectively. A massive spin s field admits $2s+1$ spin configurations characterised by the orthogonal set $\{\epsilon^{(p)}\}$, where $p \in \{-s, \dots, s\}$ is the polarisation. Then, the spin s wave function can be decomposed as

$$\Psi(t, \mathbf{x}) = \sum_p \psi_p(t, \mathbf{x}) \epsilon^{(p)}, \quad (3)$$

where ψ_p is the field with polarisation p .

In what follows we are interested in setting up the system as being composed of multiple spin s solitons in the ground state, and letting them evolve in time according to (1). For the spin 0 case, the ground state ψ_{sol} is a real function that satisfies the time-independent SP system ([Guzmán & Ureña López 2004](#)), as described in Appendix A. Without loss of generality, for higher spins we may take the ground-state of each soliton at the initial time $t = 0$ to be as in the spin 0 case equal to ψ_{sol} , multiplied by a real coefficient c_p and a phase θ_p , such that

$$\psi_p(t = 0, \mathbf{x}) = \psi_{\text{sol}}(\mathbf{x}) c_p e^{-i\theta_p}. \quad (4)$$

We assign the coefficients c_p , which determine the mixing amongst the $2s+1$ spin configurations and satisfy $\sum_p c_p^2 = 1$, and the phase $\theta_p \in [0, 2\pi)$, randomly for each soliton. A detailed description of how to compute the spherical ground state solution ψ_{sol} can be found in Appendix A.

Spin 0

This case is the simplest, and the field is defined by ψ_p in equation (4) with $c_p = 1$:

$$\psi_0 = \psi_{\text{sol}} e^{-i\theta_0}. \quad (5)$$

Spin 1

The basis is represented by the following set of orthonormal vectors, associated with three polarisation states ± 1 and 0 (Jain & Amin 2022):

$$\epsilon^{(\pm 1)} \equiv \frac{1}{\sqrt{2}} \begin{pmatrix} 1 \\ \pm i \\ 0 \end{pmatrix}; \quad \epsilon^{(0)} \equiv \begin{pmatrix} 0 \\ 0 \\ 1 \end{pmatrix}. \quad (6)$$

We assign the two c_p coefficients randomly and determine the third using $\sum_p c_p^2 = 1$ for each constructed soliton according to (4). This is equivalent to constructing orthogonal random vectors.

Spin 2

In this case, five independent states are defined by the polarisation $\pm 2, \pm 1$ and 0. The maximally polarised orthonormal tensors can be written in terms of the following orthogonal and traceless matrices

$$\begin{aligned} \epsilon^{(\pm 2)} &\equiv \frac{1}{2} \begin{pmatrix} 1 & \pm i & 0 \\ \pm i & -1 & 0 \\ 0 & 0 & 0 \end{pmatrix}, \\ \epsilon^{(\pm 1)} &\equiv \frac{1}{2} \begin{pmatrix} 0 & 0 & 1 \\ 0 & 0 & \pm i \\ 1 & \pm i & 0 \end{pmatrix}, \\ \epsilon^{(0)} &\equiv \frac{1}{\sqrt{6}} \begin{pmatrix} -1 & 0 & 0 \\ 0 & -1 & 0 \\ 0 & 0 & 2 \end{pmatrix}. \end{aligned} \quad (7)$$

This case has five c_p elements which are again assigned randomly subject to $\sum_p c_p^2 = 1$ for each soliton.

3 NUMERICAL IMPLEMENTATION

We have developed a new numerical code in C++ which solves the SP system (1) using a time-splitting pseudospectral method. For the systems under study, Fourier methods perform better than numerical local methods since the complexity is of the order of $N \log_2 N$, whereas the Finite Difference Method or the Finite Element Method has a complexity of the order of N^2 , being N the total number of operations required for each time-step (Press et al. 2007). This numerical technique has also been implemented in other works to study the evolution of the scalar field, such as Edwards et al. (2018); May & Springel (2021).

In this method, the time step Δt is expressed as a combination of operations in configuration and in Fourier space, which are applied to each component of the spin s system (2), considering that there are three and five independent terms for spin 1 and spin 2, respectively. Specifically, starting from the wavefunction $\psi_p(t, \mathbf{x})$ for each component p at time t , we first compute the $\psi_p(t + \Delta t/2, \mathbf{x})$ for each p at the half time-step $\Delta t/2$. All wavefunction components are then used for evaluating the potential $\Phi(t + \Delta t)$ by solving the Poisson

L [Mpc]	$m_s = 2.5 \times 10^{-22}$ eV	$m_s = 1.75 \times 10^{-23}$ eV
0.1	$\gtrsim 415^3$	$\gtrsim 30^3$
1	$\gtrsim 4150^3$	$\gtrsim 290^3$
10	$\gtrsim 41500^3$	$\gtrsim 2900^3$

Table 1. Minimum required number of mesh grid points N^3 for various simulation box lengths L according to (9). The estimates are shown for two scalar field masses, $m_s = 2.5 \times 10^{-22}$ eV and $m_s = 1.75 \times 10^{-23}$ eV, with the maximum velocity v_{max} set to 100km/s consistent with typical values in cosmological N-body simulations.

equation. We finally combine both steps to evaluate the wavefunction $\psi_p(t + \Delta t, \mathbf{x})$, as is captured by the following set of equations

$$\psi_p(t + \Delta t/2) = \mathcal{F}^{-1} \left[e^{-\frac{i\Delta t \tilde{\mathbf{k}}^2}{2m_s}} \mathcal{F} \left(e^{-\frac{i\Delta t \Phi(t)}{2\hbar}} \psi_p(t) \right) \right], \quad (8a)$$

$$\Phi(t + \Delta t) = \mathcal{F}^{-1} \left[-\frac{1}{\mathbf{k}^2} \mathcal{F} \left(4\pi G \rho_0 (\text{Tr}[\mathbf{\Psi}^\dagger \mathbf{\Psi}] - 1) \right) \right], \quad (8b)$$

$$\psi_p(t + \Delta t) = e^{-\frac{i\Delta t \Phi(t + \Delta t)}{2\hbar}} \psi_p(t + \Delta t/2), \quad (8c)$$

where \mathbf{k} is the spatial frequency domain, \mathcal{F} and \mathcal{F}^{-1} respectively stand for the Discrete Fourier Transformation and its inverse, and $\text{Tr}[\mathbf{\Psi}^\dagger \mathbf{\Psi}] = \sum_p \psi_p \psi_p^\dagger$, evaluated at $t + \Delta t/2$. This works because from (8c) we have that $|\psi_p(t + \Delta t)|^2 = |\psi_p(t + \Delta t/2)|^2$ so that (8b) can be consistently used. The error associated with this numerical approach is of order $\mathcal{O}(\Delta t^3)$ Glennon & Prescod-Weinstein (2021).

To obtain a robust numerical solution it is necessary to resolve the structures on the scale of the de Broglie wavelength $\lambda_{\text{dB}} = \frac{\hbar}{v}$ where $\tilde{\hbar} = \frac{\hbar}{m_s}$ and v is an estimate of the velocity of an ULDM fluid packet. We can obtain v by appealing to the Madelung representation which gives $v = \tilde{\hbar} |\nabla \alpha|$, where α is the phase of the wave function ψ and ranges between $[0, 2\pi]$. Assuming a half-step approximation for the spatial derivative, the maximum velocity that this method can resolve is estimated as $v_{\text{max}} \sim \frac{\pi \tilde{\hbar}}{\Delta x}$ (May & Springel 2021), leading to the resolution criterion

$$\Delta x < \frac{\pi \tilde{\hbar}}{v_{\text{max}}}. \quad (9)$$

Then, following the Courant-Friedrich-Lewy condition Courant et al. (1928) for parabolic equations and considering that the phase of the wave function expressed in (8) should be smaller than 2π , Δt must fulfil the condition

$$\Delta t < \min \left(\frac{4\Delta x^2}{3\pi \tilde{\hbar}}, \frac{2\pi \tilde{\hbar}}{|\Phi|_{\text{max}}} \right). \quad (10)$$

In cosmological N-body simulations $\sim 99\%$ of particles typically have velocities $v < v_{\text{max}} = 100$ km/s (May & Springel 2021). Taking this bound at face value, we display the allowed numerical resolution considering different box sizes and two different ULDM particle masses m_s in Table 1. As we see in the table, the computational power required to run large-scale simulations becomes evident.

All our simulations were performed in a cubic box of $L = 100$ kpc. To ensure good convergence we used a mesh of $N_{\text{grid}} = 512^3$ grid points in the case of spin 1 and spin 2 to be within the bounds of Table 1, corresponding to a spatial resolution of $\Delta x = 0.195$ kpc, and $v_{\text{max}} \sim 123$ km/s, as given by (9). However, as we discuss in appendices C and D, we found that when merging a large number of initial solitons this is not sufficient in the spin 0 case, but using

$N_{\text{grid}} = 1024^3$ convergence was indeed reached (corresponding to $\Delta x = 0.098 \text{ kpc}$ and $v_{\text{max}} \sim 247 \text{ km/s}$). This is because the density in the spin 0 case is typically higher and thus closer to the resolution limit compared to spin 1 and spin 2 cases where the density is distributed across two and five independent components, respectively. An analysis of the stability criteria of these configurations using different resolutions is provided in Appendix C.

Finally, we accelerated our simulations using the Fast Fourier Transformation library implemented in CUDA (cuFFT¹) for general computing on graphical processing units (GPUs). In Appendix B, we discuss briefly the performance enhancement when using GPUs.

4 MULTIPLE SOLITON MERGER

We explore the merging of an initial number of soliton configurations N_{sol} in spin 0, spin 1 and spin 2 ULDM models with otherwise equivalent initial conditions, to compare the differences they create in the resultant halo. Our methodology is generally similar to that described in Jain & Amin (2022).

4.1 Initial conditions

We ran 24 simulations for each spin s ULDM model, varying the number of solitons, N_{sol} , in steps of 5, starting from 5 up to 120. The solitons were initially positioned randomly within the subdomain $[10, 90] \text{ kpc}$, so they were sufficiently far from the boundaries, and with zero linear momentum. Each soliton configuration was generated numerically following the procedure outlined in Appendix A, with a fixed scaling factor $\lambda = 1000$ and a scalar field mass $m_s = 2.5 \times 10^{-22} \text{ eV}$. In the spin 0 case, each soliton is described as in (5) with the phase assigned randomly. For spin 1 and spin 2, each soliton is partially polarised through the linear combination given by (3) in terms of the set of maximally polarised basis defined by (6) and (7), respectively. The coefficients c_p have been assigned randomly for each soliton following (4). The mass of the soliton was computed in terms of the integrated density out to infinity, $M = \int_V \rho dV$, in isolation. Thus, all solitons have the same mass $M_{\text{sol}} = 5.31 \times 10^7 M_{\odot}$, but different polarisations c_p and phases θ_p in their wavefunction.

4.2 Evolution

4.2.1 Choosing the stopping time

For studying the final steady-state configurations, the system was allowed to evolve until a final time of $t_f = 20\tau_{\text{dyn}}$, where the dynamical time τ_{dyn} is defined as

$$\tau_{\text{dyn}} = \frac{1}{\sqrt{G\rho_0}}. \quad (11)$$

and denotes the typical timescale that a system needs to relax to an equilibrium configuration when collapsing under gravity. We show in section 4.2.2 that the system virialises after $t \sim 2\tau_{\text{dyn}}$ for each model and so taking the final configuration at $t_f = 20\tau_{\text{dyn}}$ is justified as it is more probable to lead to a stable and virialised system.

If the initial number of solitons is smaller than $N_{\text{sol}} < 5$ then $\tau_{\text{dyn}} > 30 \text{ Gyr}$ which makes the simulations computationally demanding, as we verified explicitly. We thus focus our analysis to $N_{\text{sol}} \geq 10$.

¹ <https://docs.nvidia.com/cuda/cufft/index.html>

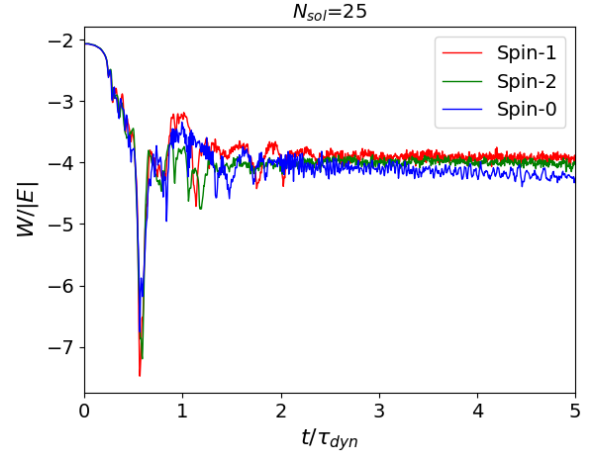


Figure 1. Evolution of the ratio $W/|E|$ as a function of t/τ_{dyn} for spin 0, spin 1 and spin 2 models with $N_{\text{sol}} = 25$.

Moreover, if $N_{\text{sol}} > 120$, then the spatial resolution and box size we use would not be enough, which sets our choice of $N_{\text{sol}} \leq 120$.

4.2.2 Energy evolution

The stability criterion of the final halo configuration in each model can be studied using the quotient $W/|E|$, where $E = W + K$ is the total energy of the system, K the kinetic energy and W the potential energy, defined as (Jain et al. 2023)

$$K = \frac{\hbar^2}{2} \int_V dV \text{Tr}[\nabla\Psi^\dagger \cdot \nabla\Psi], \quad (12)$$

$$W = \frac{1}{2} \int_V dV \Phi \text{Tr}[\Psi^\dagger \Psi]. \quad (13)$$

Fig. 1 (upper panel) shows the evolution of $W/|E|$ as a function of t/τ_{dyn} for each spin with $N_{\text{sol}} = 25$, chosen without loss of generality. The residuals with respect to the mean value of $W/|E|$, computed as a moving average, are displayed in the lower panel of the same figure. The figure displays the evolution for $t < 5\tau_{\text{dyn}}$ in order to zoom-in and emphasise the initial energy fluctuations, particularly around $t/\tau_{\text{dyn}} \sim 1 - 2$. However, the relaxation process can last for hundreds of τ_{dyn} . We observe that before the merger, the potential energy dominates, reaching a maximum value when the collision starts. After that, the three spin s models converge to a roughly constant value, with spin 0 having a slight slope. This plot demonstrates that the system slowly stabilises to a specific value of $W/|E|$ which then remains approximately constant over time. We checked that the remaining simulations with different N_{sol} exhibit similar behaviour. We note that the asymptotic value of $W/|E|$ depends also on the spin content of the initial solitons and so nothing can be said about the hierarchy observed in Fig. 1 between the three spins. Indeed, in other case of N_{sol} we have found a different hierarchy.

4.3 Properties of the resulting profiles

4.3.1 Resulting density profile

If the halo resulting from the soliton mergers is approximately spherically symmetric, we can average its density over concentric spheres. These spherical averages are shown on the left panel of Fig. 2. We then fit these averages into template functions adopting the prescription of spin 0 ULDM dark matter halos as in Schive et al. (2014a,b),

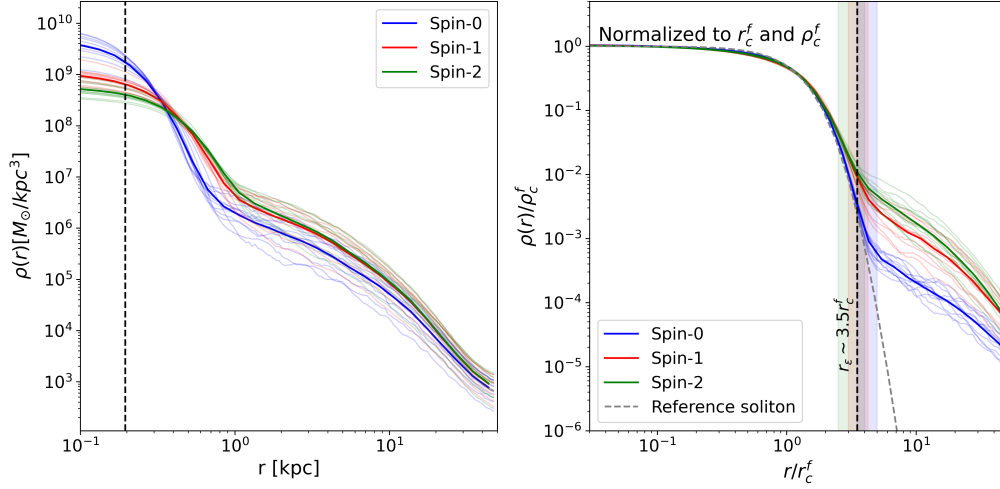


Figure 2. **Left panel.** Density profiles for each type of spin s simulation in the range $10 < N_{\text{sol}} \leq 120$, constructed via spherical averaging. The thin curves denote the density profile for a given N_{sol} for spin 0 (blue), spin 1 (red) and spin 2 (green), while the thick lines represent the average for each spin case. The vertical black dashed line represents the spatial resolution. The mass of the ULDM particles is $m_s = 2.5 \times 10^{-22}$ eV, and the mass of each soliton is $M = 5.31 \times 10^7 M_\odot$. **Right panel.** Density profile normalised by the maximum density value ρ_c^f as a function of the radius normalised by r_c^f . The soliton configuration (using $r_c = \rho_c = 1$ in (14)) is displayed for all models.

$$\rho_{\text{halo}}(r) = \Theta(r_\epsilon - r)\rho_{\text{sol}}(r) + \Theta(r - r_\epsilon)\rho_{\text{NFW}}(r), \quad (14)$$

to fit the halo density profile in each spin s model and final soliton configuration. Here, Θ is the step function, and r_ϵ is the transition radius between the soliton and the NFW tail, which are described by the following expressions

$$\rho_{\text{sol}}(r) = \frac{\rho_c}{[1 + \alpha(r/r_c)^2]^8}, \quad (15)$$

$$\rho_{\text{NFW}}(r) = \frac{\rho_s}{(r/r_s)(1 + r/r_s)^2}, \quad (16)$$

respectively, where $\alpha = 0.091$ was fixed as in Schive et al. (2014b). We defined the centre of the final solitonic core as the point with the maximum density, and used this density as the parameter ρ_c^f , where the superscript f denotes “final soliton”. The parameter ρ_s is determined through $\rho_{\text{sol}}(r_\epsilon) = \rho_{\text{NFW}}(r_\epsilon)$, so we are left with three parameters to fit: r_ϵ , r_c^f and r_s . However, naively doing this does not take into account the abrupt change from a core to an NFW profile which occurs at r_ϵ . This creates a strong degeneracy between r_c^f and r_ϵ leading to best fits which under or over-predict the profile for a range of radii in the immediate neighbourhood of r_ϵ and which are visibly distinguishable from the averaged profile. Thus our strategy was to first fit the final solitonic core (by cutting off the NFW tail) to (15) with a single parameter r_c^f , and only then fit the total profile by varying only r_ϵ and r_s . For our fits, we run Monte Carlo Markov Chain chains using the Affine Invariant Ensemble Sampler (Foreman-Mackey et al. 2013). The fits for the cases of $N_{\text{sol}} = 5$ and $N_{\text{sol}} = 120$ are shown in Fig. 3.

In Fig. 2 (left panel) we display the set of final halo density profiles for spin 0 (in blue), spin 1 (in red) and spin 2 (in green). The thin lines depict the density profile from simulations with different N_{sol} , the thick lines mark the average profile for each spin, and the vertical black dashed line denotes the numerical resolution. We observe that, within our chosen range of solitons $10 < N_{\text{sol}} \leq 120$ the profiles corresponding to each model exhibit similar behaviour, which can be effectively described by the average profile, a fact which has

potential use in observational comparisons. A noticeable difference in the shape of the profiles is observed in the central regions between spin 0 and spin 1, consistent with the findings of Amin et al. (2022). In contrast, the difference in central density between spin 1 and spin 2 is less pronounced. Increasing the spin leads to less pronounced interference patterns (see section 2.2 of Amin et al. (2022)) since the probability of constructive interference decreases with higher spin.² As the radius increases, spin 1 and spin 2 exhibit a smoother transition than the spin 0 case and the density profiles for all spins converge together at larger radii, as expected.

In Fig. 2 (right panel) we show the final density normalised with the maximum density value ρ_c^f , as a function of the radius normalised with r_c^f . Once more, the thin lines represent the scaled densities from the simulations within the set $10 < N_{\text{sol}} \leq 120$, while the dark lines mark the average density for each spin. The differences in the density profile tails are now more pronounced, with the transition from the soliton to the NFW tail being sharper for spin 0 and becoming increasingly smoother with increasing spin. We observe that the transition radius r_ϵ for these final haloes lies in the range $r_\epsilon = [2.5, 5] \times r_c^f$ represented by the blue, red and green shaded bands for spin 0, spin 1 and spin 2, respectively. The former exhibits the highest values for this quantity. The black dashed line corresponds to $r_\epsilon \sim 3.5r_c^f$, reported in Amin et al. (2022). We observe in both panels of Fig. 2 that the NFW tails for spin 0 have a wider variation around the mean than for the other spins. This occurs because the scalar field concentrates more mass in the central soliton, leading to a lower probability of occupational density in the outer regions. As a result, the tails become more diverse as the number of solitons changes. This behaviour is less pronounced in the spin 1 and spin 2 cases due to smaller interference patterns in the outer regions, leading to a smoother transition between the core and the tail, which becomes closer to the average profile regardless of the number of initial solitons.

² This is akin to what is observed in the spin 0 multi-field case, see Gosenca et al. (2023)

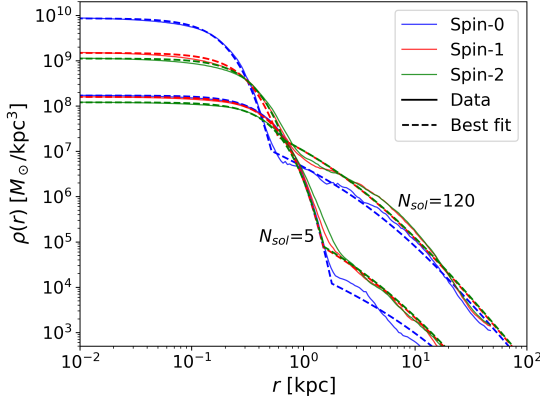


Figure 3. The solid lines represent the density of dark matter computed directly from simulations. The dashed lines shows the best fits obtained from (15) and (16) and the scaling relations discussed in section 5. For this plot, we considered two sets of simulations for $N_{\text{sol}} = 5$ and $N_{\text{sol}} = 120$.

In Fig. 3 we compare the spherically averaged halo density obtained directly from the simulations (Fig. 2) and the fits using (14). Without loss of generality, we only show the result for the lowest and highest value of the number of solitons, that is $N_{\text{sol}} = 5$ and $N_{\text{sol}} = 120$, since the rest of the simulations display a similar behaviour. We can observe a good match for both the core and the tail for simulations and fits.

4.3.2 Spin scaling relation

The spin density is defined as in Jain et al. (2023)

$$s_i = i\hbar\epsilon_{ijk}[\Psi\Psi^\dagger]_{jk}, \quad (17)$$

where $[\Psi\Psi^\dagger]_{jk} = \Psi_j\Psi_k^\dagger$ and $[\Psi\Psi^\dagger]_{jk} = \Psi_{ik}\Psi_{kj}^\dagger$ for spin 1 and spin 2 respectively. The spin angular momentum is a conserved quantity, obtained as the integral of the spin density over the volume

$$S_i = i\hbar \int_{\text{vol}} \epsilon_{ijk}[\Psi\Psi^\dagger]_{jk} dV. \quad (18)$$

Since S_i is conserved, its integral over the whole box, $|S_{\text{tot}}|$, should be the same before and after the merger.

We computed the spin density for spin 1 and spin 2 models, finding that in both cases the solitonic core is polarised, that is, s_i points to a specific direction. However, in the outer regions away from the core, s_i is randomly oriented from point to point. This agrees with and extends the results of Amin et al. (2022), which focussed on spin 1. Fig. 4 shows the relation between the spin density in the solitonic core $|S_{\text{core}}|$, defined using (18) within a spherical volume of radius $2r_c$, and the total spin $|S_{\text{tot}}|$ defined from (18) over the whole simulation volume. We normalised $|S_{\text{core}}|$ and $|S_{\text{tot}}|$ to the total number of particles $N_{\text{core}} \equiv M_{\text{core}}/m_s$ of the core and $N_{\text{tot}} \equiv M_{\text{tot}}/m_s$ of the whole simulation box, respectively. We divided the $S_{\text{tot}}/N_{\text{tot}}$ axis into 40 equal bins of width 0.025 each, and determined the average value of $S_{\text{core}}/N_{\text{core}}$ in each bin, depicted by the red and green dots, as well as the standard deviation depicted by the error bars.

We observe a rough correlation between the core $S_{\text{core}}/N_{\text{core}}$ and the total $S_{\text{tot}}/N_{\text{tot}}$ for both cases, with spin 1 reaching higher values of $|S_{\text{core}}|$ per particle. The initial assignment of spin to solitons is random and due to conservation of S_i this is reflected in the final $S_{\text{tot}}/N_{\text{tot}}$. For simulations with larger N_{sol} there is more freedom to average out the total spin angular momentum and so those typically correspond to smaller $S_{\text{tot}}/N_{\text{tot}}$. The case of spin 2 has more spin

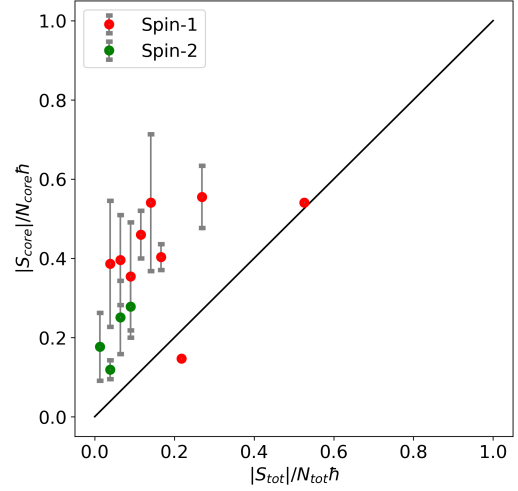


Figure 4. The normalised core spin $S_{\text{core}}/N_{\text{core}}$ versus normalised total spin $S_{\text{tot}}/N_{\text{tot}}$. The bars indicate the standard deviation for all the simulations, and the points represent the binned average data.

configurations per initial soliton than the case of spin 1, resulting in additional compactness in $S_{\text{tot}}/N_{\text{tot}}$. The solid line represents the ideal case where the spin per particle in the core is the same as the total spin and since spin 1 has denser cores than spin 2, it generally leads to higher $S_{\text{core}}/N_{\text{core}}$ reflecting a higher degree of polarisation of the final soliton.

4.3.3 Granularities

The velocity dispersion σ_v of a galactic halo provides insights into the study of the substructure and gravitational perturbations produced by dark matter density fluctuations. This phenomenon, known as dynamical heating, has been widely studied for stellar populations of galactic disks. In ULDM models, heating mechanisms can be related to subhalo perturbations or to time-dependent fluctuating substructure due to interference patterns caused by the wave nature of ULDM (Church et al. 2019). This has been particularly explored in the case of spin 0 ULDM, showing that the quantum interference patterns can be an efficient source of heating of galactic disks (Chowdhury et al. 2023; Kawai et al. 2022; Dalal & Kravtsov 2022). In higher spin ULDM models, the interference patterns are in general different, a fact which can then impact the velocity dispersion of the halo.

To study the dynamical heating process in the spin s models, we consider an idealised system of 2560 orbiting test particles representing stars orbiting inside the final halo configuration for each spin focussing on the $N_{\text{sol}} = 25$ simulation. This allows us to monitor the perturbations of the ULDM density as they impact the test particle velocities through time up to a final time of $t_f = 10\text{Gyr}$. Each star was initially placed along the x -axis (at $z = y = 0$) at different distances r_x from the centre, while having an initial velocity along the y -axis corresponding to the orbital velocity defined by

$$v_{y,\text{orbit}}(r_x) = \sqrt{\frac{GM_{\text{host}}(r_x)}{r_x}}, \quad (19)$$

where M_{host} is the enclosed mass of the ULDM host halo as a function of the radius.

The resulting σ_v of the stars for each model is shown in Fig. 5 (upper panel). To obtain the σ_v profile, the radius r was divided into

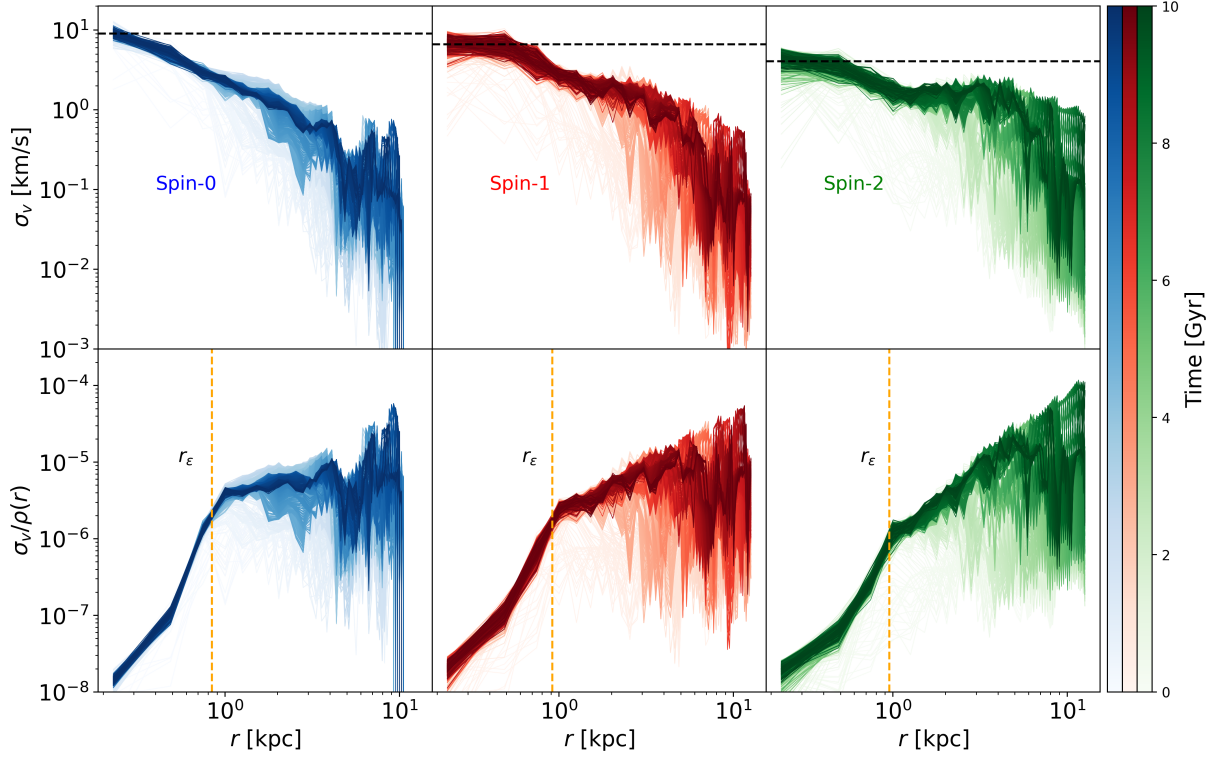


Figure 5. **Upper panel.** From left to right: evolution of σ_v corresponding to the 2560 point masses orbiting the host halo made of spin 0, spin 1 and spin 2, respectively. The black dashed lines show the temporal mean value of the velocity dispersion for all simulations in the innermost region for each model. **Bottom panel.** From left to right: The ratio $\sigma_v/\rho(r)$ corresponding to the same particles as above and compared to the dark matter profiles for $N_s = 25$ solitons for spin 0, spin 1 and spin 2. The vertical orange dashed lines mark the transition radius r_ϵ from the cored to NFW profile. The values r , σ_v and $\sigma_v/\rho(r)$ have been plotted on logarithmic scales. The colour maps for the different spins indicate how the velocity dispersion evolves, with darker colours representing later times.

bins and the average velocity dispersion was computed considering all points within each bin. The dashed lines represent the mean value of the velocity dispersion $\bar{\sigma}_v$ in the inner core the ULDM halo, for each spin s model. We observe that the particles exhibit distinct evolution for each spin due to constructive and destructive interference leading to varying perturbations in their velocity. The spin 0 case displays larger σ_v for smaller radii, which suggests that perturbations are more prominent in the central regions of the halo, consistent with it having a denser core than the other spin models; the spin 1 and spin 2 cases have hierarchically lower $\bar{\sigma}_v$ corresponding to their hierarchically lower inner core density as in Fig. 2.

The general trend in the r -dependence of the σ_v profile follows the same trend as for halo density profile within the core, that is, for $r < r_\epsilon$ it is steeper when the spin is smaller. Fluctuations become more suppressed at later times in the inner part as the collection of test particles relaxes to a steady state such that σ_v starts to follow a tighter profile with distance. This profile persists also at $r > r_\epsilon$, however, at larger distances there are large fluctuations which are likely to be numerical noise.

In the lower panel of Fig. 5 we show the ratio between the test particle velocity dispersion and the host halo density profile, $\sigma_v/\rho(r)$. Here, we can observe that this ratio increases as a function of the radius and then has a transition at r_ϵ , see (14), denoted by the orange dashed lines in each model. In the spin 0 case this ratio flattens out at $r > r_\epsilon$, while for higher spins there is a steep rise to larger distances, until the large (possibly due to noise) fluctuations spoil any visible trend. We plan to continue exploring the dynamical heating in ULDM

models in the future, in more realistic setups to get a better insight into the substructure and granularities of the ULDM configurations for each spin model, and get a better understanding on what happens at larger radii.

5 UNIVERSAL RELATIONS FOR DENSITY PROFILES OF ULDM HALOS

The SP system allows the rescaling of soliton solutions $\{M, m_s\} \rightarrow \{\lambda M, \beta m_s\}$ as

$$\{t, x, \psi, \rho\} \rightarrow \{\lambda^{-2}\beta^{-3}t, \lambda^{-1}\beta^{-2}x, \lambda^2\beta^3\psi, \lambda^4\beta^6\rho\}, \quad (20)$$

leaving the system unchanged, see (A7) in Appendix A. This leads to scaling relations which we investigate in this section, particularly their time dependence as the system relaxes towards equilibrium. For this, we use the same set of 24 simulations as in section 4. Our aim is to be able to infer the final state of the merger of an initial number of solitons, N_{sol} , using such scaling relations.

5.1 Scaling relations for central solitons

As discussed in Appendix A, the scaling symmetries of the SP system allow the rescaling of soliton solutions, in particular, a single soliton mass follows the relation $M_{\text{sol}} \rightarrow \lambda M_{\text{sol}}$. Amin et al. (2022) argue of a relation $M_{\text{sol}}^f \propto N_{\text{sol}} M_{\text{sol}}^i$ and demonstrate a tight correlation between $M_{\text{core}}/M_{\text{tot}}$ and a measure of the total energy of the system. We take

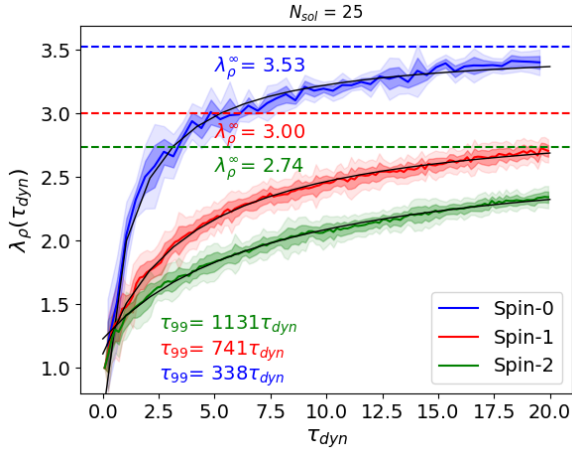


Figure 6. Time evolution of λ_ρ for $N_{\text{sol}} = 25$ until $t = 20\tau_{\text{dyn}}$. Black curves show the best fit according to (22). Dots, crosses and triangles denote data points for spin 0, spin 1 and spin 2, respectively. The horizontal dashed lines mark the λ_ρ^∞ saturation limit, assuming convergence. The value for τ_{99} , denoting the number of dynamical times required to achieve 99% of the value of λ_ρ^∞ is also displayed.

this idea further and investigate the existence of similar relations between the characteristic parameters r_c^i and ρ_c^i that describe the initial solitons with r_c^f and ρ_c^f that describe the final ULDM core, and their dependency on time until asymptotic relaxation. We focus on λ_ρ given by

$$\lambda_\rho = \left(\frac{\rho_c^f}{\rho_c^i} \right)^{1/4}, \quad (21)$$

which contains information about the halo’s characteristic maximum density.

As mergers undergo a relaxation process before forming the final halo, λ_ρ will evolve until it reaches a saturation value which is when the system is fully stabilised. We calculate λ_ρ from our simulations by tracing the maximum density in the box to define $\rho_c^f(t)$ at time t and use it in (21) along with ρ_c^i . We do this for all our 24 simulations indexed by N_{sol} and the spin. Fig. 6 displays the evolution of λ_ρ as a function of t/τ_{dyn} for the case $N_{\text{sol}} = 25$. The solid lines (blue for spin 0, red for spin 1 and green for spin 2) indicate the smoothed mean value of the λ_ρ parameter from the simulations. The dark and light-shaded regions represent 1σ and 2σ deviations, respectively. The black solid curve corresponds to the best fit using the saturation function

$$\lambda_\rho(t) = a + \frac{bt}{1+ct}. \quad (22)$$

The saturation value λ_ρ^∞ , displayed in the figure, is marked for each spin case as horizontal dashed lines. We also show τ_{99} , defined as the value of t/τ_{dyn} where λ_ρ reaches 99% of its saturation value. Appendix D displays the evolution of λ_ρ for different spatial resolutions concerning the spin 0 model. This is a consistency test to complement the discussion shown in Appendix C.

The spin 0 case has more interference patterns resulting in a higher value for λ_ρ^∞ , consistent with having higher central density as in Fig. 2. This leads to a larger saturation value λ_ρ^∞ with a steeper initial slope to reach it. This is less so for spin 1 and even less so for the spin 2 case. We also observe that the relaxation time τ_{99} shows a hierarchical behaviour, wherein the spin 0 case has the largest value,

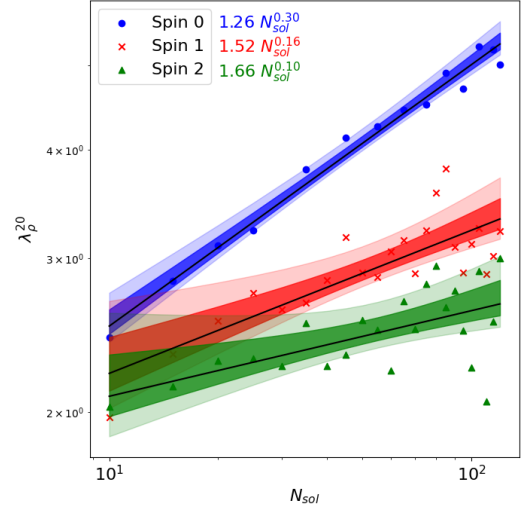


Figure 7. The scaling of λ_ρ^{20} with N_{sol} for all simulations in each spin s model. The black line corresponds to the best fit, and the dark-shaded (light-shaded) band represents the 1σ (2σ) standard deviation away from the best fit. The best fit relations are also depicted in the figure.

followed by the spin 1 and then spin 2 cases. This is verified for any number of initial solitons, not only for $N_{\text{sol}} = 25$, see Appendix E.

Additionally, we observe a monotonic increasing relation between $\lambda_\rho(t)$ and N_{sol} as a function of the dynamical time τ_{dyn} when the densities ρ_c^f and ρ_c^i were computed. In fact, if the system evolves over longer dynamical times, the mergers with higher N_{sol} will result in higher values of $\lambda_\rho^{\tau_{\text{dyn}}} \equiv \lambda_\rho(t = \tau_{\text{dyn}})$; moreover, the larger the dynamical time, the larger the density ratio $\lambda_\rho^{\tau_{\text{dyn}}}$. In Appendix E, we analyse the behaviour of $\lambda_\rho^{\tau_{\text{dyn}}}$ as a function of N_{sol} across various dynamical times. We observe a clear trend of convergence toward the asymptotic curve λ_ρ^∞ . For simplicity, we will focus on λ_ρ^{20} , in the subsequent sections.

We found that the relation of λ_ρ^{20} as a function of the number of initial solitons N_{sol} can be fit by the following power law

$$\lambda_\rho^{20}(N_{\text{sol}}) = A_\lambda N_{\text{sol}}^{B_\lambda} \quad (23)$$

with $A_\lambda = \{1.27, 1.53, 1.67\}$ and $B_\lambda = \{0.30, 0.16, 0.10\}$ for spin 0, spin 1 and spin 2, respectively. This is displayed in Fig. 7 for all three spin models. The blue points, red crosses, and green triangles represent the value of λ_ρ^{20} for spin 0, spin 1 and spin 2, for each simulation indexed by N_{sol} . The black lines represent the best fit for each model with the fitting function displayed on the figure, assuming λ_ρ depends only on N_{sol} . The dark and light-shaded regions represent the 1σ and 2σ standard deviations away from the best fit. We observe a hierarchy in the slope of the best fit between the spins, with spin 0 being the steepest. This is consistent with our findings of section 4.3.1 which indicates that the lower the spin, the more compact halos with higher central densities form by the merger of the same number of solitons.

Given the relation for λ_ρ^{20} just found and that N_{sol} is related to the total mass of the system, we may determine a scaling relation between the initial and final mass of the soliton configurations as

$$M_c^f = \lambda_\rho^{20}(N_{\text{sol}}) M_c^i. \quad (24)$$

This has the advantage being able to characterise the resulting soliton after several τ_{dyn} of evolution without the need to run the simulations.

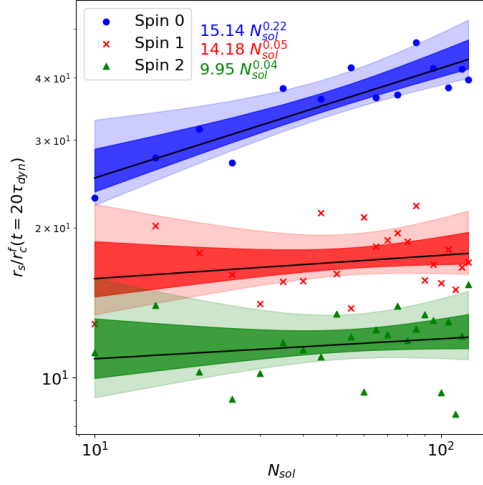


Figure 8. The scaling of r_s/r_c^f with N_{sol} for all simulations in each spin s model, computed at $t = 20\tau_{\text{dyn}}$. The black line corresponds to the best fit, and the dark-shaded (light-shaded) band represents the 1σ (2σ) standard deviation away from the best fit. The best fit relations are also shown.

5.2 Scaling relations for the NFW-tail

The outer regions of halos are characterised by an NFW tail described in (16). We explored the evolution of r_ϵ and r_s as a function of N_{sol} , evaluated at $t = 20\tau_{\text{dyn}}$, using the simulations of section 4.3.1. For this analysis, we fit first the core of the halo and then use the corresponding $r_c^f(\tau_{\text{dyn}} = 20)$ value to normalise the parameters that characterise the tail, r_s and r_ϵ .

We find that r_s/r_c^f is well fitted with the same functional form as in (23), that is, $r_s/r_c^f = A_s N_{\text{sol}}^{B_s}$, with the following values $A_s = \{15.14, 14.18, 9.9\}$ and $B_s = \{0.22, 0.05, 0.04\}$ for spin 0, spin 1 and spin 2, respectively. The result is graphically displayed in Fig. 8, where we see that spin 0 requires a significantly higher value for r_s than spin 1, which is marginally higher than the spin 2 model. This implies that mergers with the same number of solitons result in less steep tails for spin 0 compared to either spin 1 or spin 2.

Finally, r_ϵ/r_c^f is once more fitted with the same functional form as in (23), that is, $r_\epsilon/r_c^f = A_\epsilon N_{\text{sol}}^{B_\epsilon}$, with the fitting parameters taking values in $A_\epsilon = \{4.94, 5.35, 5.54\}$ and $B_\epsilon = \{-0.05, -0.013, -0.17\}$ for spin 0, spin 1 and spin 2 respectively; see Fig. 9. We see that r_ϵ is larger in the spin 0 model, followed by spin 1 and spin 2 respectively, meaning that spin 0 transitions more slowly from the solitonic core to the NFW tail.

The main conclusion from Figs. 7, 8 and 9 is that spin 0 configurations produce more compact solitons with higher central densities. These solitons enclose more mass than spin 1 and spin 2 configurations, as the transition from the soliton to the NFW tail occurs at larger radii in spin 0 models. Indeed, the lines for λ_ρ^{20} , r_s and r_ϵ do not intersect for positive values of N_{sol} , indicating that this behaviour remains consistent regardless of the number of initial configurations. Specifically, each model has distinct regions for r_ϵ , as shown by the shaded bands in Fig. 2. This suggests that the density profiles for each model display distinct characteristics that can be contrasted with observations.

Using this information, the density profile of each model can be characterised by the halo’s central density and the number of initial soliton configurations, which can even be non-integer values. In this sense, we can create equivalent halos with the same mass and corresponding density profile for each spin s model. This will be applied

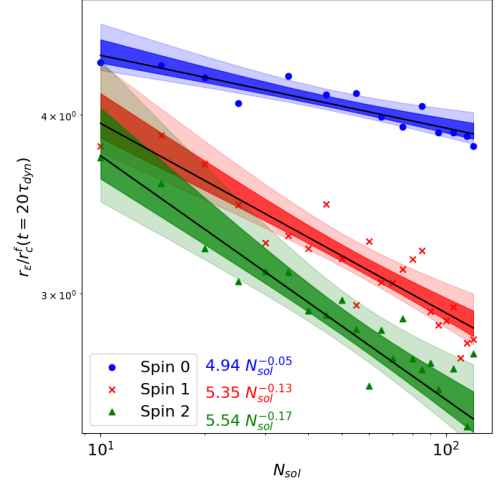


Figure 9. The scaling of r_ϵ/r_c^f with N_{sol} for all simulations in each spin s model, computed at $t = 20\tau_{\text{dyn}}$. The black line corresponds to the best fit, and the dark-shaded (light-shaded) band represents the 1σ (2σ) standard deviation away from the best fit. The best fit relations are also shown.

in the following section, using an equivalent host halo for spin 0, spin 1 and spin 2 configurations.

6 SOLITON CORES AS SATELLITE HALOS

We now turn to the question of having a satellite ULDM subhalo orbiting a host ULDM halo and consider the effects of spin on the tidal disruption of the satellite.

6.1 Constructing the system under study: host halo and satellite

To simplify our analysis we represent the host halo as an external potential calculated from the fitted ULDM profile of (14) for each spin and solve the SP system for the satellite as it interacts with this external potential. We make the additional assumption that the satellite is in a state of extreme polarisation by setting, without loss of generality, $c_D = \delta_{0D}$ in (4). That is, we are reducing the dynamics of the satellite by rotating its spin to a single relevant component. This amounts to having the satellite being described by a spin 0 ULDM soliton and this approximation is valid as long as the satellite remains isolated. Our approach is justified because as we have discussed in section 4.3.2 the halos resulting from multiple soliton mergers are highly polarised in their cores with negligible random spin density in their outer regions. Thus, the effects of spin are encapsulated in the (spin-dependent) density profile ρ_{halo} of the host halo according to (14). In all cases, we model the satellite as a spin 0 soliton with initial central density $\rho_{c,0}^{\text{sat}} = 1.37 \times 10^7 M_\odot/\text{kpc}^3$.

The dynamics of the satellite-host halo system is governed by the set of equations

$$\begin{aligned} i\hbar \frac{\partial}{\partial t} \psi &= -\frac{\hbar^2}{2m_s} \nabla^2 \psi + m_s (\Phi + \Phi_{\text{ext}}) \psi, \\ \nabla^2 \Phi &= 4\pi G \rho_0 (\psi^* \psi - 1), \end{aligned} \quad (25)$$

where Φ_{ext} is the external potential that defines the host halo. This approach has been studied analytically in Hui et al. (2017) for the spin 0 case using a simplified quadratic external potential with spherical symmetry. This was further explored through three-dimensional simulations in Du et al. (2018) solving (25) but by assuming that Φ_{ext}

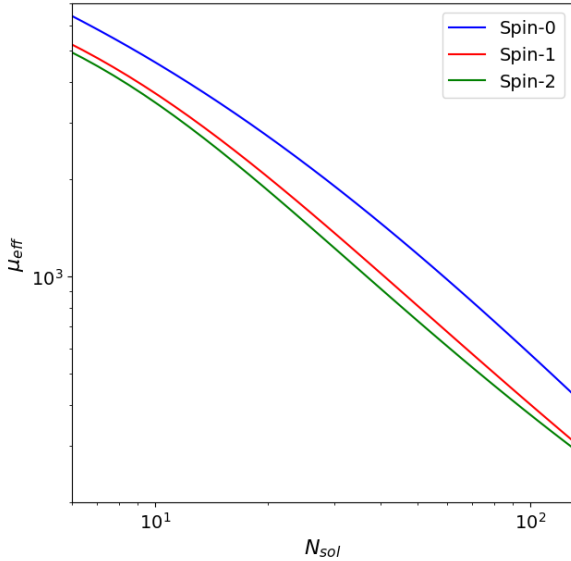


Figure 10. The dimensionless effective density parameter μ_{eff} as a function of the number of solitons N_{sol} for each spin s model. In this case, $\rho_{c,0}^{\text{sat}} = 1.37 \times 10^7 M_{\odot}/\text{kpc}^3$ and $r_{\text{sat}} = 25$ kpc are fixed.

is that of a uniform sphere with mass M_{halo} rather than a realistic ULDM profile that we use here.

We assume that host halos are described by the scaling relations described in section 5.1 along with the characterisation of the NFW tail described in section 5.2. We define the effective mean density (Du et al. 2018) of the host halo as

$$\bar{\rho}_{\text{eff}} = \bar{\rho}_{\text{halo}}(r_{\text{sat}}) - \rho_{\text{halo}}(r_{\text{sat}}), \quad (26)$$

where $\bar{\rho}_{\text{halo}}(r_{\text{sat}})$ is the average density of the halo computed until r_{sat} and use this to define the dimensionless effective density parameter μ_{eff} . This is the ratio between the initial central density of the satellite $\rho_{c,0}^{\text{sat}}$ given by (15), and $\bar{\rho}_{\text{eff}}$ as above, defined by

$$\mu_{\text{eff}} \equiv \frac{\rho_{c,0}^{\text{sat}}}{\bar{\rho}_{\text{eff}}}. \quad (27)$$

We constructed the host halos such that μ_{eff} is the same for each spin, trading N_{sol} with μ_{eff} since for a specific value of N_{sol} , and given the spin, this completely fixes the halo profile for fixed m_s and M_{sol} . The parameter μ_{eff} may be considered as a proxy for how much denser the satellite centre is compared to the halo density at that distance from the halo centre: larger μ_{eff} corresponds to denser satellites.

Fig. 10 shows the relation between μ_{eff} and N_{sol} . We observe a hierarchical behaviour across the three cases, with spin 0 exhibiting the highest value. In fact, spin 1 and spin 2 show closer values to each other compared to the first case. This is because lower spin generates denser halos, requiring fewer solitons to achieve the desired density, as explained in the previous section. Additionally, since the relations shown in section 5 are hierarchical over the simulated domain, we expect that this behaviour remains the same as N_{sol} increases, leading to a hierarchical behaviour for μ_{eff} as well. In this sense, it is possible to extrapolate this functional form to characterise more massive halos.

In Fig. 11 we show the density profiles of the host halos, ρ_{host} , for μ_{eff} in the range [30, 70], reconstructed using the scaling relations from Figures 7, 9 and 8. The lowest boundary of the shaded band represents $\mu_{\text{eff}} = 70$, the solid line at the centre corresponds to $\mu_{\text{eff}} = 50$ and the upper boundary refers to $\mu_{\text{eff}} = 30$. The main

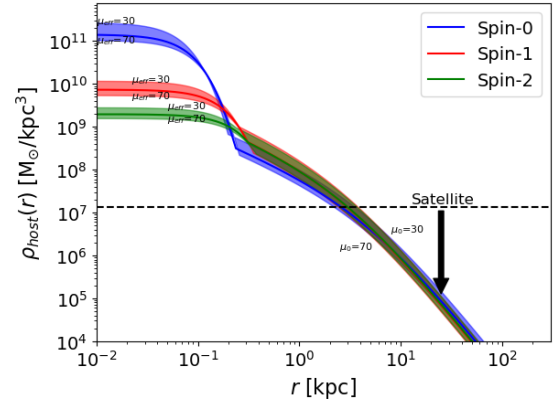


Figure 11. Density profile of the host halo reconstructed given a value of μ_{eff} in the range 30 to 70. The upper boundary of each shaded band represents $\mu_{\text{eff}} = 30$ while the lower boundary refers to $\mu_{\text{eff}} = 70$. In all cases, the initial central density of the satellite is $\rho_{c,0}^{\text{sat}} = 1.37 \times 10^7 M_{\odot}/\text{kpc}^3$. The arrow indicates the satellite's position relative to the centre of the halo and the horizontal back dashed line shows the value of $\rho_{c,0}^{\text{sat}}$.

difference in these profiles lies in the halo central densities and the transition between the core and the NFW tail. Recall that the density profile for spin 0 exhibits the most pronounced transition, more closely resembling the density of a uniform sphere, characterised by a step function with an average density $\bar{\rho}_{\text{eff}}$ for $r \leq r_*$, where r_* is the radius of the sphere.

6.2 Satellite mass-loss rate

6.2.1 Initial setup

In all cases, the satellite is described by a spin 0 soliton configuration. The only difference remains in the description of the host halo made of spin 0, spin 1 or spin 2 ULDM. We placed the satellite at a distance $r_{\text{sat}} = 25$ kpc from the centre of the host halo, represented by the arrow in Fig. 11. The coordinates are centred in the host halo, and the satellite is on the x -axis. The box size is $L = 100$ kpc with a mesh grid of $N = 512^3$. The evolution time for each simulation is determined in terms of the orbital time

$$\tau_{\text{orbit}} = \frac{2\pi r_{\text{sat}}}{v_{\text{orbit}}}, \quad v_{\text{orbit}} = \sqrt{\frac{GM_{\text{halo}}(r < r_{\text{sat}})}{r_{\text{sat}}}}, \quad (28)$$

We estimate this quantity based on Appendix C of Hui et al. (2017), where the authors estimate the number of orbits $\tau = t_{\text{disruption}}/\tau_{\text{orbit}}$ as a function of the ratio between the satellite density and the host halo. For the values of μ_{eff} in this work, the time of evolution lies within one and hundreds of orbital times. The initial velocity for the satellite is given by $\vec{v} = (0, v_{\text{orbit}}, 0)$, so that its orbit stays on the xy plane.

6.2.2 Orbital decay time

We compared the orbital time of each model to that of a uniformly dense sphere with density ρ_{halo} , such that $\mu_0 = \frac{\rho_{c,0}^{\text{sat}}}{\bar{\rho}_{\text{halo}}}$, following the approach of Du et al. (2018). Fig. 12 displays the evolution of $\rho_{c,0}^{\text{sat}}$, normalised by the initial density as a function of the number of orbits. It is evident that all models reproduce the same behaviour as the uniform sphere for a given value of μ_{eff} . It is important to highlight that these results are displayed when the host halo is considered as

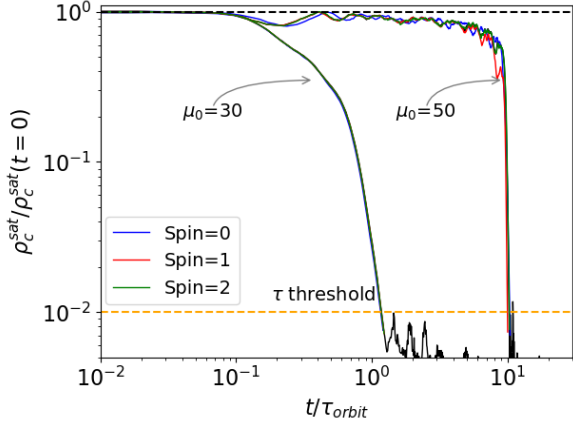


Figure 12. Evolution of the central density normalised to the initial value for $\mu_0 = 30$ and $\mu_0 = 50$ as a function of the number of orbits for spin 0 (blue), spin 1 (red) and spin 2 (green) for $\mu_{\text{eff}} = 30$ and $\mu_{\text{eff}} = 50$. The case of uniform sphere is shown in black. The black dashed horizontal line shows the difference in the initial value of the density. The yellow horizontal line shows the threshold we used to estimate the parameter τ as in Hui et al. (2017).

an external potential, this means that neither the granularities nor the direct dynamics between the host and the satellite are taken into account.

For the idealised analytical case described by Hui et al. (2017), a monotonically increasing relationship has been reported between μ_{eff} and the number of orbits before the disruption of the satellite τ , expressed as $\tau \sim e^{\mu_{\text{eff}}}$. This result was corroborated by Du et al. (2018) through 3D simulations considering the uniform sphere model mentioned earlier. Our findings demonstrate that for the case of spin- s ULDM, we can replicate the uniform sphere scenario and, consequently, the analytical result. That is, the satellite is embedded in an external potential that can be approximated by an NFW-like profile, given that most of the mass is predominantly distributed in the outer regions of the halo, making the core effects negligible.³

Given the relation between μ_{eff} and N_{sol} (see Fig. 10), we can determine the orbital decay time of a soliton surrounding an ULDM halo which can be characterised through the number of initial solitons. In fact, for the same N_{sol} the predicted orbital decay time varies depending on the model.

6.3 Equivalent astrophysical systems

In this section, we consider variations in the total mass of the halo and the fundamental mass of the ULDM theories, m_s . This allows us to analyse the dynamics of the satellite considering equivalent systems in terms of a given parameter. We will refer to the mass of the system as $M_{200} = M(r < r_{200})$ where r_{200} is the radius at which the halo’s density is $200\rho_{\text{crit}}$, with $\rho_{\text{crit}} = 127.05M_{\odot}/\text{kpc}^3$.

6.3.1 Case 1: Same core size

Our purpose here is to examine ULDM halos whose core has the same radius r_c in all cases. Although the central regions of galaxies are not yet well characterised by observations, some surveys aim to obtain more accurate measurements Hunter et al. (2012). In order

³ Indeed, Du et al. (2018) also showed that a NFW halo gives the same result as a uniform sphere.

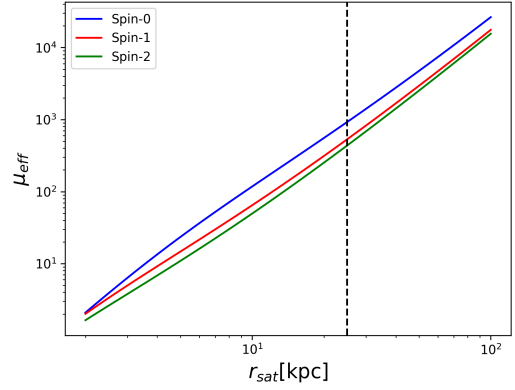


Figure 13. Relation between μ_{eff} and r_{sat} when the scaling radius is fixed to $r_c = 0.15$ kpc, which implies that the mass of the scalar field has to be modified in each case by a factor of $\beta = \{1.03, 1.25, 1.38\}$. We show the dashed vertical line at $r_{\text{sat}} = 25$ kpc to compare the different values of μ_{eff} for each model at the position of the satellite.

to keep the same value of $r_c = 0.15$ kpc in all models, we considered the scaling relation $m_{\text{ULDM}} \rightarrow \beta m_{\text{ULDM}}$ (see Appendix A). The mass of the system is $M = \{2.60, 3.29, 3.46\} \times 10^9 M_{\odot}$ and $\beta = \{1.03, 1.25, 1.38\}$ for spin 0, spin 1 and spin 2, respectively. In Fig. 13, the relation between μ_{eff} and the distance to the satellite r_{sat} is shown. We observe that μ_{eff} and thus the orbital decay time follows a hierarchical behaviour, being spin 0 the model with the largest value. Moreover, spin 1 and spin 2 show more similar values of μ_{eff} over the entire domain. This means that in this case, the satellite will survive longer orbiting a halo made of spin 0 ULDM compared to a halo with the same core size but different ULDM spin.

6.3.2 Case 2: Same M_{200}

In this case we instead rescale M_{200} of the ULDM halo so that it is the same across all models. This approach can be applied to astrophysical systems, where the halo mass has been inferred by considering precise measurements of the galactic components. The scaling relation to consider is $M_{200} \rightarrow \lambda M_{200}$, with $\lambda = \{0.38, 0.30, 0.29\}$ for spin 0, 1 and 2, respectively. The initial mass for each halo are $M_{200} = \{2.60, 3.29, 3.46\} \times 10^9 M_{\odot}$, giving a mass of $M = 1 \times 10^9 M_{\odot}$ after the transformation. Fig. 14 shows the relation between μ_{eff} and the distance to the satellite within the same range as in case 1). Here, we observe an inverted hierarchy where μ_{eff} become more similar as r_{sat} increases. In this case, spin 2 shows the highest value of the orbital decay time.

7 CONCLUSION

We performed numerical simulations for spin 0, spin 1 and spin 2 ULDM models, finding important differences between them for virialised systems. First, the resulting halos from merging multiple solitons exhibit notable variations in the density profiles. The spin 0 model always produces denser, more compact cores with a more prominent transition between the soliton and the NFW-tails. In contrast, the halos formed in the spin 1 and spin 2 models share more similarities, featuring less dense central cores and less extended envelopes with smoother transitions. This is attributed to interference effects, as higher spin values reduce the probability of having fully constructive or destructive interference. Indeed, these similarities

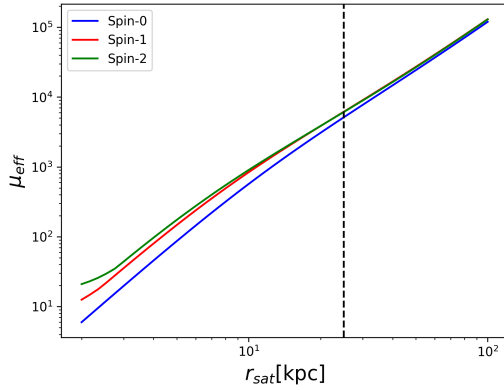


Figure 14. Relation between μ_{eff} and r_{sat} when $M_{200} = 1 \times 10^9 M_{\odot}$ is fixed for all models for the same range as in Fig. 13. In this case the halos must be rescaled by a factor of $\lambda = \{0.38, 0.30, 0.29\}$. The dashed black line represent the position of the satellite.

persist across all the scaling relations observed for the density profile parameters: spin 0 consistently differs significantly from spin 1 and spin 2. The general shape of the halos remains consistent regardless of the number of solitons involved in the merger. These distinct characteristics allow for clear differentiation between the spin s models, providing a valuable framework for comparison with observational data. Notice that in this work we have limited ourselves to ULDM without self-interactions. We expect that the introduction of the self-interactions will make the differences between spins more prominent, because different polarisations in the SP system (1) will couple to each other directly, rather than simply through the common gravitational potential Φ . We leave this possibility for future work.

The resultant halos have been used to study the inner substructure and granularities of the DM configurations in each model through the velocity dispersion of test particles orbiting through the system. We found that the velocity dispersion decreases for larger spin since the central density for spin 0 is lower than spin 1 and spin 2, and the interference patterns are fewer for spin 1 and spin 2 than in the spin 0 case. This result might relax the constraints on the mass of the ULDM candidates arising from the dynamical heating of stellar systems. Indeed, for the spin 0 case, it has been argued that for masses below $\sim 10^{-19}$ the dynamical heating would increase the velocity dispersion in ultra-light dwarf galaxies to values much larger than what is observed (Chowdhury et al. 2023; Dalal & Kravtsov 2022). This limit could be alleviated for ULDM with higher spin. In order to test this effect, we plan to perform more realistic simulations considering a galactic disk in future works.

By varying the parameters of our simulations, we identified universal scaling relations that characterise both the central core and the external envelope of the resulting halos based on the initial solitons involved in the merger. These relations are expressed as a function of the number of solitons, which may be non-integer. Using this information, it is possible to determine the free parameters of the ULDM halo profile for a fixed halo mass, including the characteristic core radius r_c , the transition parameter r_{ϵ} , the envelope radius r_s and maximum density ρ_c . This allows for the generation of equivalent configurations for the three models in terms of mass or average density, which is valuable for comparative analysis. Additionally, these parametric relations can be used to characterise profiles at different simulation stages, helping reduce computational costs. For example, running cosmological simulations up to a high redshift, such as $z > 3$, can be computationally efficient. From there, the profile parameters

can be determined by extrapolation, allowing further analysis without requiring extensive simulation time. In the near future we will extend this framework by conducting simulations within an expanding Universe.

Thanks to the scaling relations we identified, we constructed equivalent host halos for each spin s model and considered them as external potentials to study the dynamics of solitonic satellites. The most remarkable finding is that the satellite dynamics is invariant to the spin of the ULDM candidate provided the average density of the halo is identical across all models. As a result, the orbital decay time is the same in all cases. Additionally, when considering equivalent ULDM halos with the same core size, we find that the orbital decay time is longer for spin 0. However, when fixing the total mass of the halo, the satellite survives longer for the spin 2 model. These findings are relevant in order to observationally discriminate between models. Consider for instance the so-called timing problem of some dwarf satellite galaxies such as Fornax, which hosts several globular clusters. In CDM models a prominent dark matter halo can cause such globular clusters to experience significant dynamical friction, leading them to spiral inwards and eventually merge with the galaxy’s centre over time. Therefore, the survival time of these systems is much shorter than the proposed age of the galaxy. Implementing ULDM models with different spin present a wide phenomenology for the satellite systems by allowing differences in the number of orbits before being disrupted. For the particular case with the same core size we observe that higher spins are not favoured since they show lower orbital decay times. On the other hand, if we consider the same total mass, then spin 2 shows a higher value for the time which could relax the tension. Therefore, to draw more accurate conclusions it is necessary to identify observables which allow us to characterise dark matter halos to construct systems in each model that are equivalent in terms of these observables.

In summary, spin 1 and spin 2 ULDM models can help resolve some of the problems that have been discussed for spin 0 ULDM simulations. The first concerns the cores of halos observed in some galactic systems. While all three models form a core, in the spin 0 case the core has higher central densities. Veltmaat et al. (2020) demonstrated that including baryons leads to cuspy scalar dark matter profiles, thereby reintroducing the tension with observational data that ULDM was thought to cure. This problem can be relaxed if the resultant halos have lower central densities, as seen in the spin 1 and spin 2 models. The second problem is related to the discrepancy between the predicted velocity dispersion in spin 0 models and observations. Higher-spin models could help resolve this tension by predicting lower values for this quantity. Finally, in the case of satellite systems, spin ULDM models may predict longer orbital decay times, depending on the specific characteristics of the host halo, which can be contrasted with observations of dwarf spheroidal galaxies.

ACKNOWLEDGEMENTS

We wish to thank our HPC staff Josef Dvořáček for technical support throughout this project and Mustafa Amin for valuable correspondence. The research leading to these results has received support from the European Structural and Investment Funds and the Czech Ministry of Education, Youth and Sports (project No. FORTE—CZ.02.01.01/00/22_008/0004632). FU and CS acknowledge support from MEYS through the INTER-EXCELLENCE II, INTER-COST grant LUC23115. CS acknowledges support from the Royal Society Wolfson Visiting Fellowship “Testing the properties of dark matter with new statistical tools and cosmological data”. This article is based

upon work from the COST Action COSMIC WISPerS CA21106, supported by COST (European Cooperation in Science and Technology).

DATA AVAILABILITY

The evolution of the energies of the 24 simulations for each spin, the spherically averaged density profiles (as shown in Fig. 2) and the scaling relations discussed in sec. 5 are available in Zenodo, at <https://doi.org/10.5281/zenodo.14791353>

REFERENCES

- Adshead P., Lozanov K. D., 2021, *Physical Review D*, 103
- Alexander S., Jenks L., McDonough E., 2021, *Physics Letters B*, 819, 136436
- Amin M. A., Jain M., Karur R., Mocz P., 2022, *Journal of Cosmology and Astroparticle Physics*, 2022, 014
- Bertone G., Tait T. M. P., 2018, *Nature*, 562, 51–56
- Bullock J. S., Boylan-Kolchin M., 2017, *Annual Review of Astronomy and Astrophysics*, 55, 343
- Chen J., Du X., Zhou M., Benson A., Marsh D. J. E., 2023, *Phys. Rev. D*, 108, 083021
- Chowdhury D. D., van den Bosch F. C., van Dokkum P., Robles V. H., Schive H.-Y., Chiueh T., 2023, *The Astrophysical Journal*, 949, 68
- Church B. V., Mocz P., Ostriker J. P., 2019, *Monthly Notices of the Royal Astronomical Society*, 485, 2861
- Courant R., Friedrichs K., Lewy H., 1928, *Mathematische Annalen*, 100, 32
- Dalal N., Kravtsov A., 2022, *Physical Review D*, 106, 063517
- Del Popolo A., Le Delliou M., 2017, *Galaxies*, 5
- Du X., Schwabe B., Niemeyer J. C., Bürger D., 2018, *Physical Review D*, 97, 063507
- Edwards F., Kendall E., Hotchkiss S., Easter R., 2018, *Journal of Cosmology and Astroparticle Physics*, 2018, 027
- Feng J. L., 2010, *Annual Review of Astronomy and Astrophysics*, 48, 495–545
- Ferreira E. G. M., 2021, *The Astronomy and Astrophysics Review*, 29
- Foreman-Mackey D., Hogg D. W., Lang D., Goodman J., 2013, *Publ. Astron. Soc. Pac.*, 125, 306
- Glennon N., Prescod-Weinstein C., 2021, *Phys. Rev. D*, 104, 083532
- Gorghetto M., Hardy E., March-Russell J., Song N., West S. M., 2022, *Journal of Cosmology and Astroparticle Physics*, 2022, 018
- Gosenca M., Eberhardt A., Wang Y., Eggemeier B., Kendall E., Zagorac J. L., Easter R., 2023, *Phys. Rev. D*, 107, 083014
- Guzmán F. S., Ureña-López L. A., 2004, *Phys. Rev. D*, 69, 124033
- Guzmán F. S., Ureña-López L. A., 2003, *Physical Review D*, 68, 024023
- Hu W., Barkana R., Gruzinov A., 2000, *Phys. Rev. Lett.*, 85, 1158
- Hui L., Ostriker J. P., Tremaine S., Witten E., 2017, *Phys. Rev. D*, 95, 043541
- Hunter D. A., et al., 2012, *The Astronomical Journal*, 144, 134
- Jain M., Amin M. A., 2022, *Physical Review D*, 105
- Jain M., Amin M. A., Thomas J., Wanichwecharungruang W., 2023, *Phys. Rev. D*, 108, 043535
- Kawai H., Oguri M., Amruth A., Broadhurst T., Lim J., 2022, *The Astrophysical Journal*, 925, 61
- Lancaster L., Giovanetti C., Mocz P., Kahn Y., Lisanti M., Spergel D. N., 2020, *JCAP*, 01, 001
- Matos T., Guzman F. S., Urena-Lopez L. A., 2000, *Class. Quant. Grav.*, 17, 1707
- May S., Springel V., 2021, *Monthly Notices of the Royal Astronomical Society*, 506, 2603
- Niemeyer J. C., 2020, *Progress in Particle and Nuclear Physics*, 113, 103787
- Press W. H., Teukolsky S. A., Vetterling W. T., Flannery B. P., 2007, *Numerical Recipes 3rd Edition: The Art of Scientific Computing*, 3 edn. Cambridge University Press, USA
- Schive H.-Y., Chiueh T., Broadhurst T., 2014a, *Nature Physics*, 10, 496
- Schive H.-Y., Liao M.-H., Woo T.-P., Wong S.-K., Chiueh T., Broadhurst T., Hwang W. Y. P., 2014b, *Phys. Rev. Lett.*, 113, 261302
- Tulin S., Yu H.-B., 2018, *Physics Reports*, 730, 1

- Veltmaat J., Schwabe B., Niemeyer J. C., 2020, *Phys. Rev. D*, 101, 083518
- Vitsos A., Gourgouliatos K. N., 2023, *Journal of Cosmology and Astroparticle Physics*, 2023, 071

APPENDIX A: GROUND STATE SOLITON

For spin 0 particles, the system of equations (1) is reduced to the well-known Schrödinger-Poisson system

$$i\hbar \frac{\partial}{\partial t} \psi = -\frac{\hbar^2}{2m_s} \nabla^2 \psi + m_s \Phi \psi \quad (\text{A1})$$

$$\nabla^2 \Phi = 4\pi G |\psi|^2.$$

In spherical coordinates, the Laplacian can be expressed as

$$\nabla^2 f = \left(\frac{\partial^2}{\partial r^2} + \frac{2}{r} \frac{\partial}{\partial r} \right) f + \frac{1}{r^2 \sin \theta} \frac{\partial}{\partial \theta} \left(\sin \theta \frac{\partial}{\partial \theta} \right) f + \frac{1}{r^2 \sin^2 \theta} \frac{\partial^2}{\partial \varphi^2} f,$$

where θ and φ are the polar and azimuthal angles. After assuming spherical symmetry, we can drop the angular dependency. Then, the Schrödinger-Poisson system takes the form

$$\frac{\hbar^2}{2m_s} \frac{\partial^2}{\partial r^2} (r\psi_{\text{sol}}) = r\psi_{\text{sol}}(m_s \Phi - \mu c^2), \quad (\text{A2})$$

$$\frac{\partial^2}{\partial r^2} (r\Phi) = 4\pi G r \psi_{\text{sol}}^2. \quad (\text{A3})$$

It is convenient to rewrite the system of equations using the following transformations $\hat{\psi}_{\text{sol}} = \frac{\sqrt{G}}{\hbar} \psi_{\text{sol}}$ and $\hat{\Phi} = \frac{\Phi}{\hbar^2}$. Then, we have

$$\frac{1}{2} \frac{\partial^2}{\partial r^2} (r\hat{\psi}_{\text{sol}}) = r\hat{\psi}_{\text{sol}}(\hat{\Phi} - \hat{\mu}), \quad (\text{A4})$$

$$\frac{\partial^2}{\partial r^2} (r\hat{\Phi}) = 4\pi r \hat{\psi}_{\text{sol}}, \quad (\text{A5})$$

where $\tilde{\hbar} = \frac{\hbar}{m_s}$ and $\hat{\mu} = \frac{m_s \mu c^2}{\hbar^2}$ is a constant which corresponds to the eigenvalue of the system (A4). Since we are looking for equilibrium configurations, we consider the following conditions

$$\begin{aligned} \hat{\psi}_{\text{sol}}(r \rightarrow \infty) &\rightarrow 0, & \hat{\Phi}(r \rightarrow \infty) &= -\frac{GM}{\tilde{\hbar}^2 r}, \\ \hat{\psi}(r \rightarrow 0) &= 1, & \left. \frac{\partial \hat{\Phi}}{\partial r} \right|_0 &\rightarrow 0, \\ \left. \frac{\partial \hat{\psi}}{\partial r} \right|_0 &\rightarrow 0, & \left. \frac{\partial \hat{\psi}}{\partial r} \right|_{r \rightarrow \infty} &\rightarrow 0, \end{aligned} \quad (\text{A6})$$

with $M(r) = \int \rho dV = 4\pi \int \rho(r) r^2 dr$ is the enclosed mass at radius r and $\rho/\rho_0 = |\psi|^2$. By setting these conditions, there are unique values of μ and $\Phi(0)$ for which the boundary conditions are fulfilled. Also, the SP system is invariant under the rescaling relations given by $\{M, m_{\text{ULDM}}\} \rightarrow \{\lambda M, \beta m_{\text{ULDM}}\}$

$$\{t, x, \psi, \rho\} \rightarrow \{\lambda^{-2} \beta^{-3} t, \lambda^{-1} \beta^{-2} x, \lambda^2 \beta^3 \psi, \lambda^4 \beta^6 \rho\}. \quad (\text{A7})$$

We can find solutions for this system for a fixed value of the ULDM mass, as shown in Fig A1. See Amin et al. (2022); Guzmán & Ureña-López (2003) for further details.

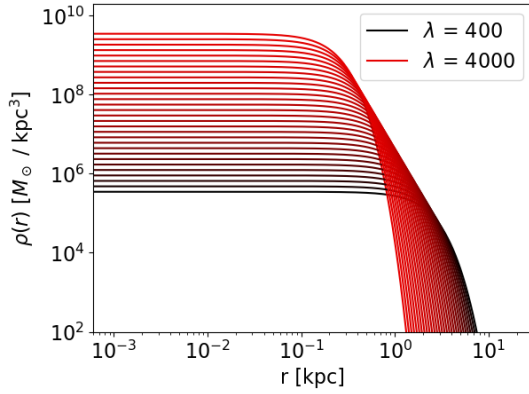


Figure A1. Ground state solution for the time-independent SP system considering $m = 2.5 \times 10^{-22}$ eV. The different colours show different values for the scaling parameter λ to highlight the differences in the central and outer regions described in equation (A7). In this paper we fixed $\lambda = 1000$ for all the solitonic configurations used.

APPENDIX B: PERFORMANCE OF THE CODE

To test the efficiency of the code, we have performed 1000 Fourier transformations using different mesh sizes to compare the execution time for two methods. The first one uses FFTW-MPI with different numbers of cores (2, 32, 256 and 1024), while the second one uses cuFFT on a single Nvidia A100 GPU with 80GB of memory. Fig. B1 shows the speedup of each method, defined as the ratio of its execution time to the execution time when using a single CPU. Theoretically, the speedup is expected to match the number of cores used. However, the process is inefficient due to communication between cores and memory allocation. The remarkable improvement the GPU provides becomes evident as the number of mesh grid points increases, significantly benefitting the type of simulations conducted in this work. The GPU performance is one order of magnitude larger than the MPI version.

One disadvantage of GPUs is their limited memory, whereas FFTW-MPI depends on RAM for memory allocation, which is usually larger than GPUs. We thus plan to use the MPI version of cuFFT (cuFFTMp) to increase allocation capacity in a future work.⁴ Additionally, it is worth mentioning that we have parallelised the FFTW-MPI library for only one axis. Further improvements could involve parallelising in two dimensions, leading to better performance. There are publicly available tools, like 2decomp-fft, that can be used for this purpose.⁵

APPENDIX C: STABILITY CRITERION FOR THE GPP SYSTEM (CONSERVATION OF ENERGY)

In Fig. C1, the evolution of the ratio $\Delta E/E_0$ over time is shown for 20 solitons, where $\Delta E = E(t) - E_0$ with E_0 the energy at $t = 0$. Here $E = K + W$, where the kinetic and potential energies are defined in (12) and (13), respectively. This is presented for two different spatial resolutions, $N_{\text{grid}} = 256^3$ and $N_{\text{grid}} = 512^3$, for spin 0 (blue line), spin 1 (green line) and spin 2 (red line). The algorithm we apply, also known as a kick-drift-kick method, has second-order error $O(2)$ for the temporal step. Ideally, the energy should remain constant, with

⁴ <https://docs.nvidia.com/hpc-sdk/cufftmp/index.html>

⁵ <https://github.com/2decomp-fft/2decomp-fft>

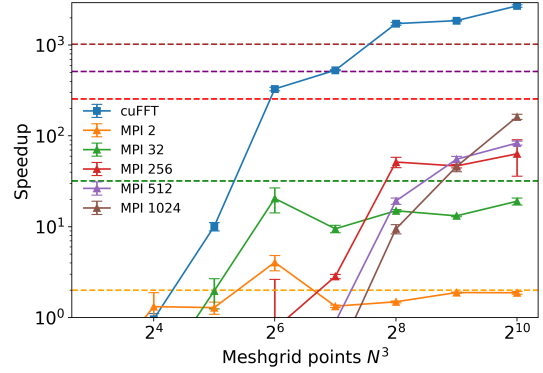


Figure B1. Comparison of the performance between the Fastest Fourier Transform in the West (FFTW) library using MPI with 2, 32, 256 and 1024 cores, and CUDA FFT (cuFFT) library on a single CPU. In all cases, the speed was computed relative to the performance of a single core. Horizontal dashed lines indicate the expected ideal performance for MPI.

$\Delta E = 0$. However, some errors arise due to the finite approximation of the wave function. Our code demonstrates convergence as we increase the spatial resolution from 256^3 (dashed lines) to 512^3 (solid lines), with an exponential decrease in error. The spin 0 case (blue) exhibits the most significant error propagation, primarily due to denser and narrower structures forming, which will require much more resolution than in the other models. In contrast, the spin 2 case (red) shows lower error propagation, given that the central density of these halos is smaller. As expected, all three spin s ULDM models converge to zero at the highest resolution. This works as a consistency test of the conservation of energy, with better convergence for lower resolutions in the case of higher spin, since constructive interference becomes less likely. Consequently, the spin 0 model will require higher resolution than spin 1 and spin 2, and the effects of varying resolutions will be more pronounced in the first case. The behaviour for a different number of solitons is similar.

Additionally, we tested the energy stability of the system by following the ratio $W/|E|$ over time. We considered two different mesh resolutions 512^3 and 1024^3 . Fig. C2 shows the $W/|E|$ ratio using $N_{\text{grid}} = 512^3$ for the three models and $N_{\text{grid}} = 1024^3$ for spin 0 only. In all cases, $N_{\text{sol}} = 55$ was considered. We found that, while for spin 0 there is a break in the curve due to the resolution, spin 1 and spin 2 show well-defined convergence behaviour. This becomes more evident for larger values of N_{sol} . In fact, we can reproduce the same behaviour using both resolutions for spin 0 if $N_{\text{sol}} < 30$. That is, below this threshold it is valid to use both spatial resolutions for the three models. As mentioned in section 4.1, the spin 0 model requires higher resolution because it has only one component for the density, which could lead to larger values near the resolution limit. This issue is not present in the other models, where the wavefunction can be split into more components. Therefore, using $N_{\text{grid}} = 512$ for spin 1 and 2 is sufficient, and increasing the resolution would be unnecessarily computationally expensive.

APPENDIX D: RESOLUTION TESTS FOR λ_ρ

As a complement of Appendix C, we compare the evolution of λ_ρ as a function of τ_{dyn} using both resolutions for the spin 0 model with $N_{\text{sol}} = 25$. This value of N_{sol} lies within the range where both resolutions, $N_{\text{grid}} = 512^3$ and $N_{\text{grid}} = 1024^3$, converge and satisfy the stability criterion. (see Appendix C). In Fig. D1, we present λ_ρ

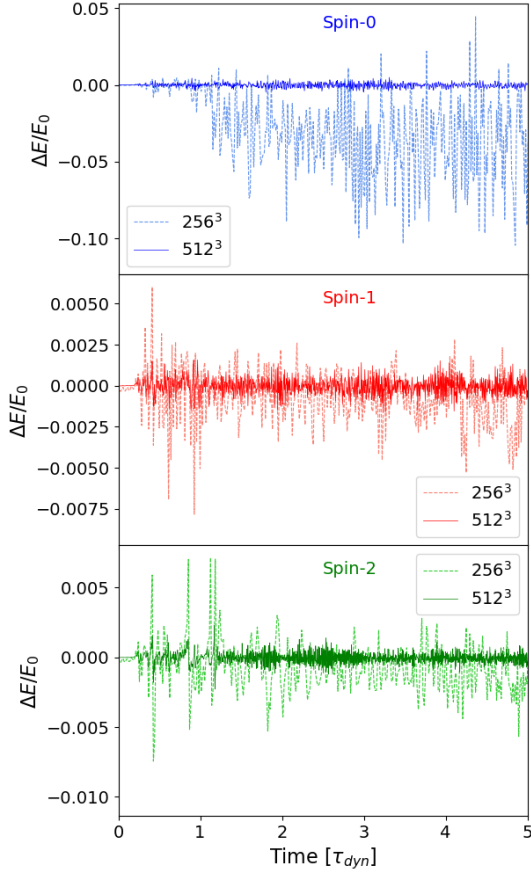


Figure C1. Energy variation as a function of time for spin 0 (top, blue), spin 1 (middle, green) and spin 2 (bottom, red) considering a merger of $N_{\text{sol}} = 20$, without loss of generality.

for both cases, showing a similar behaviour for both scenarios. The corresponding values of λ_ρ^∞ for each case are also included. Beyond $N_{\text{sol}} > 30$, there is no convergence for λ_ρ with $N_{\text{grid}} = 512^3$.

APPENDIX E: CONVERGENCE RATE FOR λ_ρ^∞

This section presents the evolution of λ_ρ as a function of N_{sol} for different dynamical times. In Fig. D2, we observe the curves for this quantity at $t = \{5, 20, \infty\}\tau_{\text{dyn}}$, for the spin-0 (left), spin 1 (centre) and spin 2 (right) models. We found that the larger the dynamical time at which the densities from (21) were computed, the greater the corresponding value of λ_ρ for the same N_{sol} . The saturation value is reached when $t \rightarrow \infty$. Due to computational limitations, in this work, we limit the simulations to $20\tau_{\text{dyn}}$ to perform the fits discussed in Sec. 5. Additionally, we considered more than $5\tau_{\text{dyn}}$, since for the larger N_{sol} , the systems show that they satisfy the energy relaxation criteria, but some solitons still stay in orbit. On the other hand, we also observe that, for the same dynamical time, λ_ρ is higher the lower the spin, due to the prominent cores for the spin 0 model, showing a very defined hierarchical evolution for this quantity.

This paper has been typeset from a \LaTeX file prepared by the author.

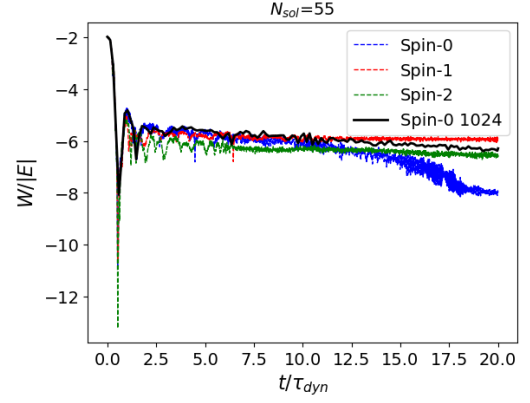


Figure C2. Evolution of the ratio $W/|E|$ as a function of t/τ_{dyn} for spin 0, spin 1 and spin 2 models with $N_{\text{sol}} = 55$ (within the range where the stability criteria is not fulfilled for $N_{\text{grid}} = 512^3$). The blue, red and green lines corresponds to spin 0, spin 1 and spin 2 with a resolution of $N_{\text{grid}} = 512^3$. The black lines refers to the spin 0 model with $N_{\text{grid}} = 1024^3$.

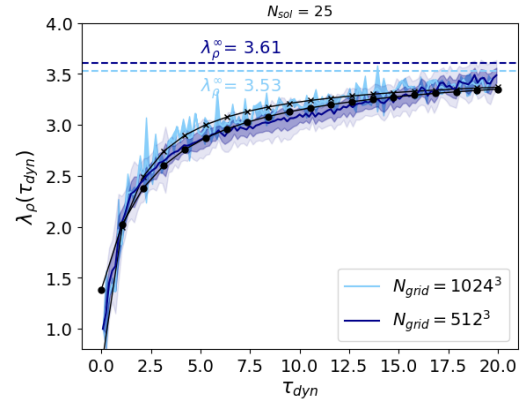


Figure D1. Evolution of λ_ρ as a function of τ_{dyn} for spin 0 considering two different resolutions for the simulation, 512^3 and 1024^3 for $N_{\text{sol}} = 25$ (within the range where the stability criteria of energy is fulfilled for both resolutions). The convergence value at infinity is also shown for both cases.

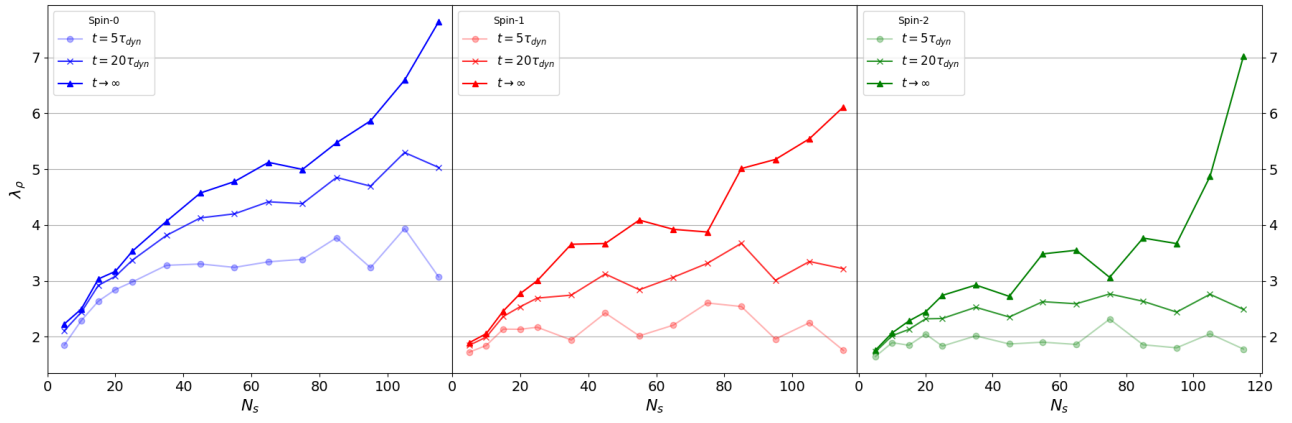


Figure D2. From top to bottom: Evolution of λ_ρ for different N_{sol} for $t = \{5, 20, \infty\}\tau_{\text{dyn}}$ for spin 0 (left), spin 1 (centre) and spin 2 (right).